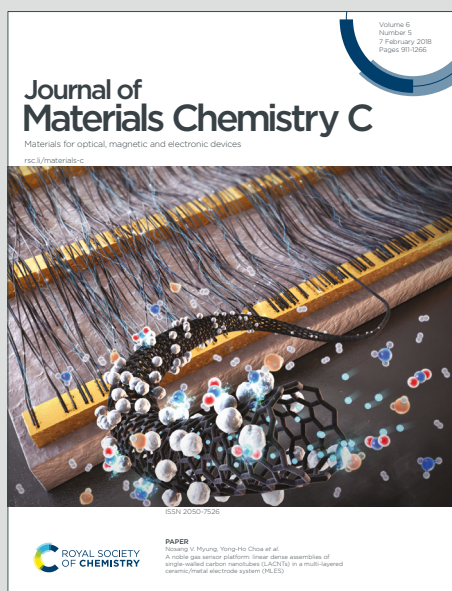


Journal of Materials Chemistry C

Materials for optical, magnetic and electronic devices

Accepted Manuscript

This article can be cited before page numbers have been issued, to do this please use: O. Ola, H. Ullah, Y. Chen, K. Thumavichai, N. Wang and Y. Zhu, *J. Mater. Chem. C*, 2021, DOI: 10.1039/D1TC01022K.



This is an Accepted Manuscript, which has been through the Royal Society of Chemistry peer review process and has been accepted for publication.

Accepted Manuscripts are published online shortly after acceptance, before technical editing, formatting and proof reading. Using this free service, authors can make their results available to the community, in citable form, before we publish the edited article. We will replace this Accepted Manuscript with the edited and formatted Advance Article as soon as it is available.

You can find more information about Accepted Manuscripts in the [Information for Authors](#).

Please note that technical editing may introduce minor changes to the text and/or graphics, which may alter content. The journal's standard [Terms & Conditions](#) and the [Ethical guidelines](#) still apply. In no event shall the Royal Society of Chemistry be held responsible for any errors or omissions in this Accepted Manuscript or any consequences arising from the use of any information it contains.

ARTICLE

DFT and Experimental Studies of Iron Oxide-based Nanocomposites for Efficient Electrocatalysis

Oluwafunmilola Ola,^a Habib Ullah,^b Yu Chen,^c Kunyapat Thumavichai,^d Nannan Wang,^d and Yanqiu Zhu^{c*}Received 00th January 20xx,
Accepted 00th January 20xx

DOI: 10.1039/x0xx00000x

The synthesis of iron oxide nanoparticles coated with graphitic carbon nitride ($\text{Fe}_x\text{-NC}$), and their improved electrochemical stability and corrosion resistance in acidic electrolyte environment are reported. Our results show that the $\text{Fe}_x\text{-NC}$ nanocomposites exhibit enhanced activity and long-term stability for HER in 0.5 M H_2SO_4 aqueous solution, with an onset potential of 73 mV and Tafel slope of 69 mV dec^{-1} . Furthermore, DFT calculations are carried out to represent our experimental system. Both theory and experiment strongly correlate with each other, where $\text{gC}_3\text{N}_4@\text{FeO}$ has superior performance to the pristine gC_3N_4 . It is found that the electrocatalytic activity of $\text{gC}_3\text{N}_4@\text{FeO}$ arise from the electron transfer from FeO particles to the gC_3N_4 which form an electrostatic interaction, leading to a decreased local work function on the surface of gC_3N_4 . The resulting graphitic carbon nitride shells prevented the direct contact between iron oxide nanoparticles and acidic electrolyte (H_2SO_4), so that the improved stabilities and corrosion resistance could be achieved. This work sheds light on new efficient and durable electrocatalysts for applications in acidic environments.

Introduction

Water electrolysis has attracted a wide attention as a promising approach for generating high energy density hydrogen at high conversion efficiencies with zero CO_2 emissions. Hydrogen evolution reaction (HER) which represents the cathodic half reaction of water electrolysis requires electrocatalysts to simultaneously increase the reaction rate and efficiency while lowering the overpotential. Among many electrocatalysts, the platinum group of metals have been remaining as the first choice due to their fast kinetics, almost thermoneutral hydrogen binding energy ($G \sim 0$) and hydrogen evolution at values close to reaction's equilibrium potential.¹ However, the high cost and scarcity of platinum-based materials have intensified the research of alternative low-cost electrocatalysts, to drive the transition to a viable hydrogen economy. Recent progress has focused on the development of traditional electrocatalysts and corresponding hybrids using metal/non-metal compounds of nitrides, selenides, phosphides, and carbides. The synthesis of low-cost, yet effective HER catalysts remain a major challenge. Some of the strategies for improving

HER catalytic activity include heteroatom doping, particle size and morphology modification and incorporation of metal/oxide nanoparticles in carbon-based materials. Although much progress has been made in promoting higher HER activity, most of these materials are unstable under acidic and alkaline conditions, since they mainly rely on the interaction of metal-H bonds for HER.²

The encapsulation of nanosized electrocatalyst by carbon-based materials such as graphene has been proposed as a means of improving catalytic activity, efficiency, and stability, because graphitic carbon shells have high electrical conductivity, large surface area, good chemical stability, excellent structural tunability and particularly good insolubility in many solvents. These features are linked to improved electron transfer at exposed catalytic active sites under extreme operational conditions.² Furthermore, these graphitic carbon shells have also been reported to enhance HER activities by altering the Gibbs free energy of hydrogen adsorption through interaction between metal/metal oxide compounds and the surrounding carbon shell. These carbon shells can effectively prevent direct contact between metal atoms and electrolytes, so that the stability and corrosion resistance of electrocatalysts can be improved. Further introduction of single or multiple heteroatoms of nitrogen (N),³ phosphorus (P),⁴ and boron (B)⁵ into the carbon shells can tune the electronic conductivity by offering improved charge transfer, thus influencing the electrocatalytic performance.

Iron and its derivatives are attractive for electrocatalysis due to their low cost and relative abundance.⁶⁻⁹ However, their catalytic activity is limited due to instability and deactivation

^a Faculty of Engineering, The University of Nottingham, University Park, Nottingham, NG7 2RD, United Kingdom

^b Renewable Energy Group, College of Engineering, Mathematics and Physical Sciences, University of Exeter, Penryn Campus, Cornwall TR10 9FE, United Kingdom

^c College of Engineering, Mathematics and Physical Sciences, University of Exeter, EX4 4QF, United Kingdom

^d Key Laboratory of New Processing Technology for Nonferrous Metals and Materials, Ministry of Education, School of Resources, Environment and Materials, Guangxi University, Nanning, China

*Corresponding author. Tel: +44 1392 723620. E-mail: Y.Zhu@exeter.ac.uk.

Electronic Supplementary Information (ESI) available: [details of any supplementary information available should be included here]. See DOI: 10.1039/x0xx00000x



ARTICLE

resulting from leaching of active nanoparticles from reaction medium. Encapsulating iron and its derivatives in heteroatom doped carbon shells prepared by the chemical vapor deposition and self-templating technique can influence the catalytic activity while facilitating improved electron transfer, faster hydrogen desorption and better stability.² Herein, we use melamine as a nitrogen and carbon source to create such sheathed iron-oxide nanoparticles for electrocatalysis. The new process is an inexpensive and scalable method which is realized via a simple carbonization under inert atmosphere. Experimental results show that iron oxide nanoparticles encapsulated in graphitic carbon nitride shell can work as an efficient HER catalyst in an acidic medium with activities that are comparable to other reported carbon encapsulated catalysts.

Experimental

Preparation of Fe_x-NC nanocomposites

Fe_x-NC samples were prepared via dip coating and carbonization. Varying amounts of Fe (C₅H₅)₂ (Sigma Aldrich) precursor were dissolved in ethanol (Sigma Aldrich) to obtain homogeneous solutions. Melamine-formaldehyde (MF) sodium bisulfite foams (Avocation Ltd) were then dip-coated in the precursor solutions of different concentrations (0.02 - 0.1 M). The dip-coated foams were dried overnight at 80 °C and then carbonized at 800 °C under continuous argon flow of 50 mL min⁻¹. Approximately 50 mL min⁻¹ of hydrogen gas was introduced into the furnace at the target temperature of 800 °C for 30 min to obtain the final samples. The as-prepared samples were denoted as Fe_x-NC where x represents the concentration of Fe, such that precursor solution concentration varied at 0.02 M, 0.05 M, and 0.1 M was named as Fe₂-NC, Fe₅-NC and Fe₁₀-NC, respectively.

Characterization and Electrochemical Testing

The morphology and structures of the samples were characterized using scanning electron microscope (Hitachi S3200N, Oxford instrument - SEM-EDS) operated at 20 kV and JEOL-2100 high-resolution transmission electron microscope (HR-TEM) operated at 200 kV. X-ray diffraction (XRD) patterns were acquired on a Bruker D8 Advance diffractometer (operated at 40 kV, 40 mA), with a Cu K α radiation, at a step size and dwell time of 0.02° and 1 s respectively. Raman spectrum was recorded on a Renishaw RA800 series benchtop system with a 532 nm excitation length under a laser power of 6 mW. X-ray photoelectron spectra (XPS) were recorded using a VG ESCALab Mark II spectrometer with a non-monochromatic Al-anode X-ray source (1486.6 eV), operated at a 12-kV anode potential and a 20-mA filament emission current. N₂ adsorption/desorption was determined by Brunauer Emmet Teller (BET) measurements using a Quantachrome Autosorb-IQ surface area analyser. Information on the chemical bonding was obtained using attenuated total reflectance-Fourier transform infrared spectroscopy (ATR-FTIR, Bruker) over a wavelength of 400-4000 cm⁻¹. A CHI-760D electrochemical workstation with a three-electrode system was used to evaluate the

electrocatalytic activity of the nanocomposites. The CHI-760D workstation was coupled with a rotating disk electrode (RDE) system where the reference, counter and working electrodes were Ag/AgCl/KCl, platinum wire and glassy carbon electrode (GCE) covered with catalyst ink, respectively. The catalyst ink was prepared via ultrasonification of a mixture of 5 μ L of Nafion solution, 1 mL of ethanol/water solution and 3 mg of Fe_x-NC sample. The measurements (cyclic voltammograms, linear sweep voltammograms and impedance spectroscopy) were carried out in a 0.5 M H₂SO₄ (Sigma Aldrich) electrolyte solution at different potentials and scan rates varying from 0 - -0.8 V and 10 - 100 mV, respectively. The electrode was calibrated by a reversible hydrogen electrode (RHE) and acquired data were corrected for iR losses. Optimal sample was further subjected to stability test for 5000 cycles.

Computational Methodology

In order to support our experimental data, DFT simulation was performed on QuantumATK¹⁰ while visualizations are achieved on VESTA and vnl Version 2019.12.¹¹ To model the experimentally g-C₃N₄ encapsulated FeO_x nanoparticles, two different strategies are employed; **(I)** g-C₃N₄ is built where mixture of Fe₃O₄ and Fe₂O₃ (collectively denoted as FeO) are encapsulated to form g-C₃N₄@FeO (Figure 1a, b), and **(II)** a single layer of g-C₃N₄ is incorporated on the surface of Fe₃O₄ (Figure 1c-e).

Model (I): DFT calculation are performed to understand the origin of the HER activity of g-C₃N₄@FeO. Although the sizes of the FeO nanoparticle and g-C₃N₄ considered in the calculations are much smaller than the FeO nanoparticles and g-C₃N₄ observed experimentally, the essential effect on the electronic structure, as shown below, can already be captured by this simple geometry. The supercell g-C₃N₄ is in rectangular lattice which replicates four-unit cells of the bare tube in c direction; the vacuum thicknesses in a and b directions are set to ~15 Å to avoid interactions between g-C₃N₄. A 1x1x5 Monkhorst-Pack k-point sampling for the structural relaxation has been employed,

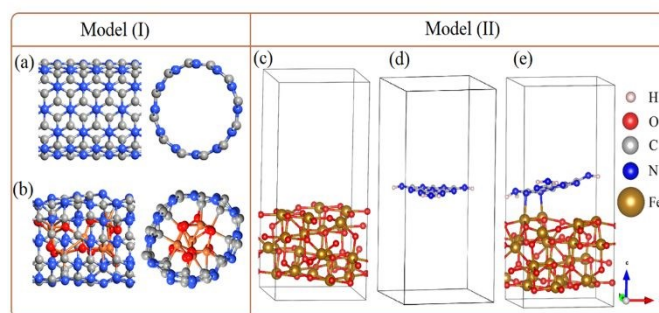


Figure 1. Optimized geometric structures of g-C₃N₄ front and side view (a), g-C₃N₄ encapsulated FeO nanoparticles with front and side view (b), optimized geometric structures of Fe₃O₄ (c) monolayer of g-C₃N₄ (d), and Fe₃O₄@g-C₃N₄ (e).

while a uniform k-point grid such as 5x5x5 is used for the electronic property simulations. The details of hydrogen adsorption and Gibbs free energy methodologies are given in the Supporting Information.



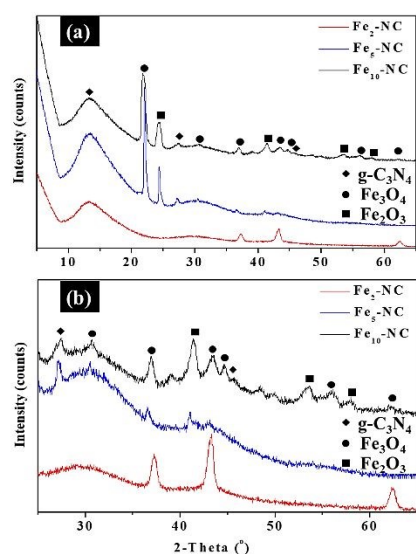


Figure 2. XRD patterns of Fe_x-NC samples (a), with enlarged patterns of iron oxides (b).

Model (II): We also performed DFT simulations for the second model where magnetite Fe₃O₄ with a cubic space group of Fd3m is considered.¹² The lattice parameters of magnetite Fe₃O₄ are $a/b/c = 8.394 \text{ \AA}$ and $\alpha/\beta/\gamma = 90$. After optimizing the lattice parameters of 56 atoms of bulk Fe₃O₄; a Fe₃O₄(001) slab was built. For the slab model calculations of surface energies and band edge positions, the thickness of the slab was kept as enough to ensure that the centre of the slab can be regarded as the bulk phase. A vacuum space of about 10 Å was kept between slabs, to eliminate the fictitious interaction between the periodically repeating slabs. After surface stability confirmation of Fe₃O₄(001), a single layer of g-C₃N₄ is incorporated on its surface to build the Fe₃O₄(001)@g-C₃N₄, as shown in Figure 1c. Hereafter, the Fe₃O₄(001) will be denoted as Fe₃O₄ and Fe₃O₄(001)@g-C₃N₄ as Fe₃O₄@g-C₃N₄. Finally, two water molecules were interacted on the optimized surfaces of Fe₃O₄ and Fe₃O₄@g-C₃N₄, to determine the HER efficiency in the form of water adsorption energy. Generalized gradient approximation (GGA) with the Perdew Burke Ernzerhof (PBE) exchange-correlation functional and double Zeta Polarized (DZP) basis set is used for the structural and energy optimization due to its superiority over hybrid pseudopotentials.¹³ Moreover, a linear combination of atomic orbitals (LCAO) method is used for Fe, O, C, N, and H atoms.¹⁴

Results and Discussion

Structural and Physicochemical Properties

Fe_x-NC samples were evaluated by XRD to determine the phase purity and crystalline structure. Figure 2 shows the XRD pattern which confirms the presence of graphitic carbon nitride (g-C₃N₄) and iron oxides. Two characteristic peaks of g-C₃N₄ at 13.6° and 27.4° are indexed to the (100) and (002) planes which is linked to the in-planar structure of the tri-s-triazine ring and interplanar stacking peak of C-N systems, respectively.¹⁵

Besides g-C₃N₄, diffraction peaks of Fe_x-NC samples are in good

DOI: 10.1039/D1TC01022K

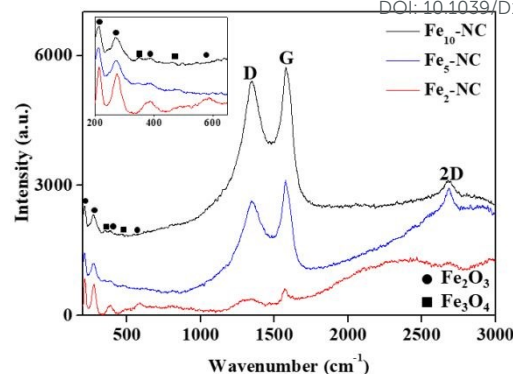


Figure 3. Raman spectra of Fe_x-NC samples with inset showing corresponding iron oxides.

agreement with the standard pattern of cubic spinel Fe₃O₄ (PDF 2107249). The XRD profile shows the complete phase transformation of Fe (C₅H₅)₂ to α-Fe₂O₃ after thermal decomposition at 800 °C. Further phase transformation of α-Fe₂O₃ to Fe₃O₄ was observed for Fe₂-NC, with mixtures of rhombohedral α-Fe₂O₃ (PDF 1011267) and cubic Fe₃O₄ being observed for Fe₅-NC and Fe₁₀-NC samples prepared at higher precursor concentration. The presence of zero valent iron or iron carbide species was not observed.

Besides g-C₃N₄, diffraction peaks of Fe_x-NC samples are in good agreement with the standard pattern of cubic spinel Fe₃O₄ (PDF 2107249). The XRD profile shows the complete phase transformation of Fe (C₅H₅)₂ to α-Fe₂O₃ after thermal decomposition at 800 °C. Further phase transformation of α-Fe₂O₃ to Fe₃O₄ was observed for Fe₂-NC, with mixtures of rhombohedral α-Fe₂O₃ (PDF 1011267) and cubic Fe₃O₄ being observed for Fe₅-NC and Fe₁₀-NC samples prepared at higher precursor concentration. The presence of zero valent iron or iron carbide species was not observed.

The Raman spectra of Fe_x-NC samples, presented in Figure 3, show the characteristic peaks of graphene, α-Fe₂O₃ and Fe₃O₄, and further confirm the successful formation of Fe_x-NC nanocomposites. For carbon, the identified peaks of the D peak (~1350 cm⁻¹), G peak (~1580 cm⁻¹) and 2D peak (~2690 cm⁻¹) are linked to defects, bond stretching of sp² graphitic carbon atom and high-energy second-order process of graphene, respectively. The peak intensity ratio of D band to G band is calculated to be 0.89, 0.88 and 0.94 for Fe₂-NC, Fe₅-NC and Fe₁₀-NC, respectively. The higher peak intensity ratio of Fe₁₀-NC depicts the presence of higher structural defects compared with other Fe_x-NC samples. Characteristic peaks of Fe₂O₃ and Fe₃O₄ were also observed and marked in the spectra. Raman shifts at ~212, 274, 389 and 586 cm⁻¹ are assigned to A_{1g} and E_g modes of Fe₂O₃.¹³ The two additional peaks at 329 and ~497 cm⁻¹ confirmed the presence of Fe₃O₄.⁶

The ATR-FTIR spectra of Fe₅-NC are shown in Figure S1. Absorption peaks at the 2115 and 2350 cm⁻¹ region were observed which is due to the C≡N stretching.^{17, 18} The



ARTICLE

1994 cm^{-1} peak is linked to bridge carbonyl groups.¹⁶ The prominent bands at 462, 550 and 602 cm^{-1} are attributed to Fe–O vibrational modes in $\alpha\text{-Fe}_2\text{O}_3$.¹⁹ The weak peak at 630 cm^{-1} is attributed to the stretching vibration mode of the Fe–O bonds in the crystalline lattice of Fe_3O_4 .²⁰

The SEM and TEM images of $\text{Fe}_x\text{-NC}$ samples are displayed in Figure 4. As shown in the SEM images (Figures 4a, 4c and 4e), the $\text{Fe}_x\text{-NC}$ consists of nanotubes of several micrometers in length with varying diameters, which were grown on the surface of carbon foams. Based on SEM elemental analysis, all $\text{Fe}_x\text{-NC}$ samples are composed of C, N, O and Fe elements which are uniformly distributed. TEM images of single $\text{Fe}_x\text{-NC}$ nanocomposites prepared with varying precursor concentration are shown in Figures 4b, 4d and 4f. The outer diameter of the nanotubes was measured at about 47–117 nm with a wall thickness of 8.1–30 nm. The inner/outer diameter and wall thickness of the nanotubes were observed to decrease with increased precursor concentrations.

The enlarged TEM image shows that nanoparticles are encapsulated within the nanotubes (Figures 4b, 4d and 4f).

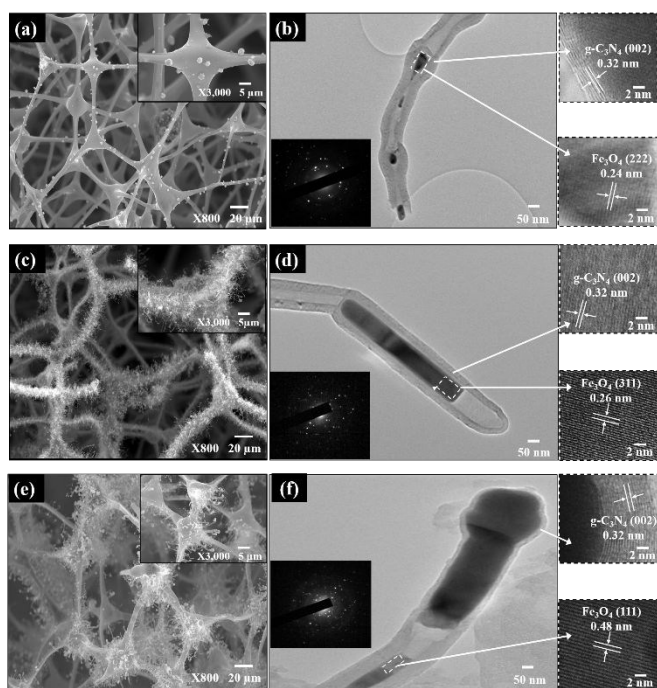


Figure 4. SEM, HRTEM, and SAED morphological and structural characterisation of $\text{Fe}_x\text{-NC}$ samples: (a-b) $\text{Fe}_2\text{-NC}$, (c-d) $\text{Fe}_5\text{-NC}$, (e-f) $\text{Fe}_{10}\text{-NC}$ [Zoomed zones in (b, d and f) showing the lattice spacing of $\text{Fe}_x\text{-NC}$ samples].

High-resolution TEM (HRTEM) image shows that the outer layer of the nanotubes consists of graphitic layers with an interlayer spacing of 0.32 nm linked to (002) plane of $\text{g-C}_3\text{N}_4$. Individual spots seen in the SAED patterns also indicates that $\text{Fe}_x\text{-NC}$ samples consist of mainly iron oxide nanoparticles. HRTEM image of the nanoparticle marked with a rectangle shows lattice fringes with d-spacing of 0.24, 0.26 and 0.48 nm corresponding to the (222), (311) and (111) planes of Fe_3O_4 nanoparticles for $\text{Fe}_2\text{-NC}$, $\text{Fe}_5\text{-NC}$ and $\text{Fe}_{10}\text{-NC}$, respectively.^{6, 21, 22} Based on the

above analyses, we believe that the crystalline Fe_3O_4 nanoparticles were encapsulated in multi-walled nanotubes and the size of the encapsulated nanoparticles varies from a few to hundreds of nanometers.

The presence and distribution of C, N, O and Fe elements were also confirmed by TEM elemental mapping in Figure 5. All the elements were well distributed in the $\text{Fe}_{10}\text{-NC}$. The atomic contents of $\text{Fe}_{10}\text{-NC}$ sample quantified by TEM-EDS are 90, 0.4, 2.5 and 7.1 at % for C, N, O and Fe, respectively, which shows a Fe:O ratio close to 3:1. Indeed, the XRD and Raman results (Figures 2 and 3) confirmed that the nanoparticles in $\text{Fe}_x\text{-NC}$ could exist as either Fe_2O_3 or Fe_3O_4 species. As shown in Figure 5, highly uniformly distributed C and N species existed around the iron oxide particle at nanoscale, confirming that the iron oxides were completely encapsulated in the carbon/nitrogen shell. BET and pore size distribution analyses were conducted, and the resulting specific surface area of $\text{Fe}_2\text{-NC}$, $\text{Fe}_5\text{-NC}$ and $\text{Fe}_{10}\text{-NC}$ was 368, 476 and 223 $\text{m}^2 \text{g}^{-1}$, respectively. The mesoporous features of the samples are shown in Figure S2.

The surface bonding configurations and chemical composition of the samples were evaluated by XPS, and the results are shown in Figure S3-4 and 6. The survey spectrum confirms the

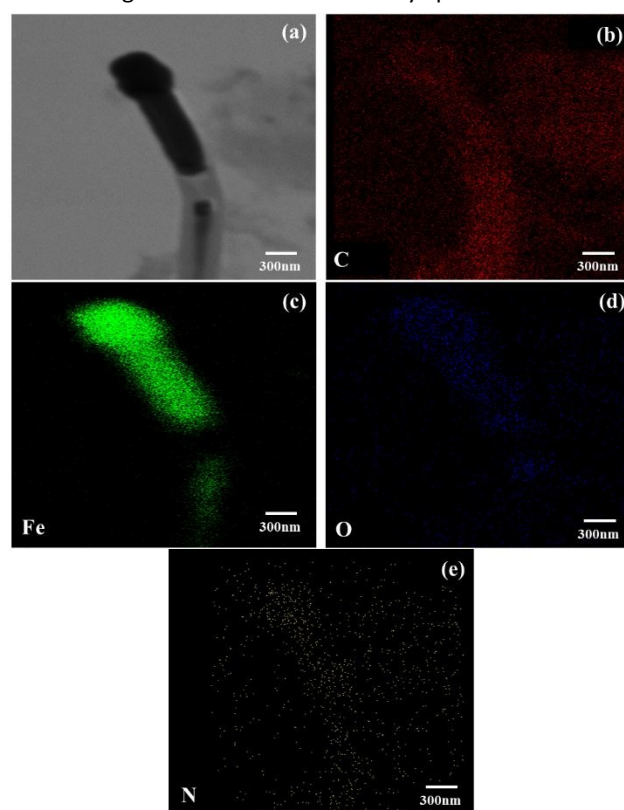


Figure 5. (a) A TEM image of sample $\text{Fe}_{10}\text{-NC}$ and (b-e) its corresponding EDS elemental mapping for C, Fe, O and N, as marked.

presence of C, N, O and Fe in all samples, in accordance with the SEM and TEM-EDS results. The composition of C, N, O and Fe is 83, 2, 7 and 8 wt % for $\text{Fe}_5\text{-NC}$, respectively (Figure S3a). The results of other $\text{Fe}_x\text{-NC}$ samples investigated by XPS are



summarized in Table S1. Comparison of the relative N and Fe elemental abundances indicates that Fe₁₀-NC contains ~4 wt % N and ~14 wt % Fe on the surface.

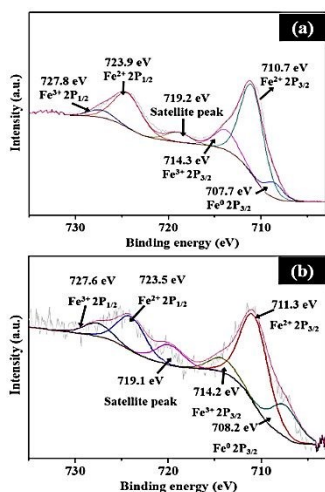


Figure 6. XPS spectrum of Fe 2p for Fe₅-NC, (a) before and (b) after cyclic HER testing.

As shown in Figure S3b, the XPS spectra of C 1s are fitted into five components, assigned to C-C (284.5 eV), C=N (285 eV), C=O (287.6 eV), O-C=O (289.4 eV), and C π (291.3 eV).²³ The main peak at 284.5 eV is linked to sp² carbon which shows that the carbon content of the samples is predominantly graphitic in nature. As shown in Figure 6a, the high-resolution XPS spectra of Fe show peaks at 711.3 and 714.2 eV which can be assigned to the binding energies of the 2p_{3/2} orbitals of Fe²⁺ and Fe³⁺ species, respectively. For the 2p_{1/2} orbital, the peaks at 723.5 and 727.6 eV are attributed to the binding energy of Fe²⁺ and Fe³⁺ species, respectively. The peak at 719.1 eV is a satellite peak while additional peak at 708.2 eV is linked to metallic Fe. The Fe 2p_{3/2} peak at 711.3 eV indicates Fe-N bonding as Fe ions are coordinated to N.²⁴ XPS studies of Fe₅-NC before and after testing in Figure 6b shows similar peaks, however, a negligible

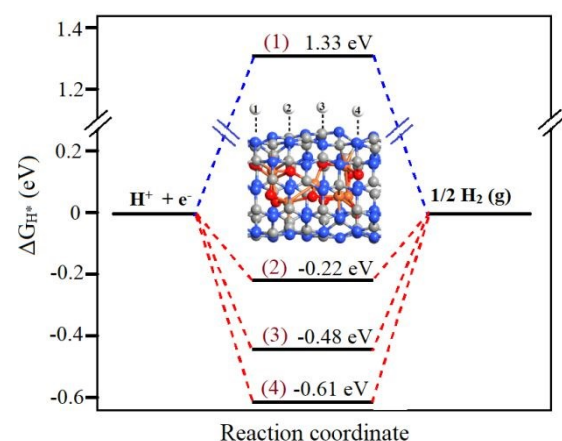


Figure 7. Gibbs free energy (ΔG_{H^*}) of HER process on four different positions of g-C₃N₄@FeO. Inset shows the four different positions, where H is attached; on position (1) and (4) H is attached to N while at (2) and (3) H is attached to C of g-C₃N₄@FeO.

change in relative proportion of Fe species on the active Fe₅-NC electrode after cyclic HER studies are observed.

Deconvolution of the high-resolution XPS O1s peak confirmed the presence of oxygen related to the iron oxide catalyst (529.8 eV) and some carboxylic and hydroxyl species on the surface of Fe₅-NC sample at 533.1 and 531.5 eV, respectively (Figure S3c). N 1s spectra were deconvoluted into three peaks which are assigned to the pyridinic N (398.3 eV), graphitic N (401.0 eV), and quarternary N⁺ - O⁻ (402.8 eV) with atomic contents of 26, 57 and 16 at % (Figure S3d). Pyridinic N serves as metal-coordination sites due to their lone-pair electrons while graphitic N was reported as catalytically active sites for electrocatalysis.²⁵ These two types of N species are of high content in Fe_x-NC samples, which potentially lead to a high catalytic activity.

First-Principles Electronic Properties

Model (I): g-C₃N₄ Encapsulated Fe₂O₃/Fe₃O₄ (g-C₃N₄@FeO):

To determine the Gibbs free energies (ΔG_{H^*}) of hydrogen adsorption, we choose the first model of g-C₃N₄@FeO. First-principles DFT calculations are employed to simulate the ΔG_{H^*} adsorption on g-C₃N₄@FeO (Figure 1a-b), the clusters of Fe₂O₃ and Fe₃O₄ nanoparticles are given in Figure S5b, c of the Supporting Information. The calculated ΔG_{H^*} values on four different positions of g-C₃N₄@FeO are marked as position 1 - 4 and plotted in Figure 7. The ΔG_{H^*} value at position 1-4 are 1.33, -0.22, -0.48, and -0.61 eV, respectively. Comparative analysis of

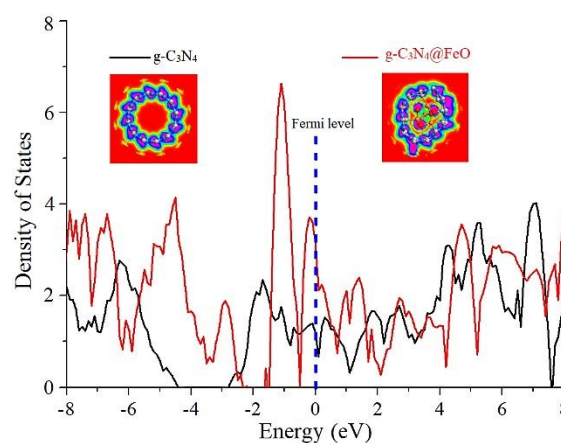


Figure 8. Comparative density of states plots of g-C₃N₄ and g-C₃N₄@FeO. The Fermi energy level is aligned at 0 eV. Insets show the electron difference density (EDD) of pristine SWNCNT and g-C₃N₄@FeO.

Figure 7 leads us to predict that the ΔG_{H^*} value at position (2) is optimum (-0.22 eV), responsible for dissociation reaction, and shows higher catalytic activity. The reason behind this activity is due to the electrostatic bonding of H with the C atom of g-C₃N₄@FeO. On the other hand, the ΔG_{H^*} value at position number (4) is maximum (-0.61 eV) which is due to the strong adsorption energy of H atom over the surface of catalyst. This higher adsorption energy does not dissociate the hydrogen bonding and decreases the overall catalytic activity. Moreover,



ARTICLE

the ΔG_{H^*} value at position (1) is positive (1.33 eV) and here the H is also attached to N of g-C₃N₄@FeO. However, the N atom of g-C₃N₄@FeO has no bonding with Fe of FeO. In this case, no association takes place and consequently, there will be no HER as well. Furthermore, the ΔG_{H^*} values of H adsorption at position (3) is -0.48 eV, which is also higher and does not allow dissociation reaction. In summary, the H-N interaction at position (4) is stronger which is due to the direct contact of Fe of FeO with N of g-C₃N₄. The ΔG_{H^*} value at position (2) exhibits high activities toward HER which is close to the thermodynamic limit value of 0 and even far better than that of the Pt (111) surface, which is ~0.09 eV.²⁶ The reason behind this is the encapsulation of FeO with g-C₃N₄ and to avoid its direct contact with the H atoms which slightly minimizes the adsorption energy. So, we propose that g-C₃N₄@FeO-based electrocatalysts are promising candidates for highly efficient HER. Furthermore, we suggest that the enhanced HER activity of g-C₃N₄@FeO is due to the encapsulation of FeO nanoparticles with the g-C₃N₄ shell which has affected the properties of the wall where H is adsorbed (see Figure 7).

The density of states (DOS) of pristine g-C₃N₄ is compared with that of g-C₃N₄@FeO and shown in Figure 8, where the interaction of Fe-C, Fe-N, O-C, and O-N in g-C₃N₄@Fe can be identified. The DOS of g-C₃N₄@FeO is enhanced especially near the valance band (0 to -1.8 eV) which is due to the interaction of C and N atoms with FeO clusters and exhibit extra features near the Fermi level. Moreover, charge transfer also occurred from the FeO cluster to the g-C₃N₄ which raises the Fermi level by about 0.12 eV. This effect is further illustrated by the electron difference density (EDD) distribution as shown in the inset of Figure 8. The charge transfer creates a local dipole near the interface which consequently decrease the local work function and increase the chemical reactivity of the functionalized region of the g-C₃N₄@FeO exterior. So, this

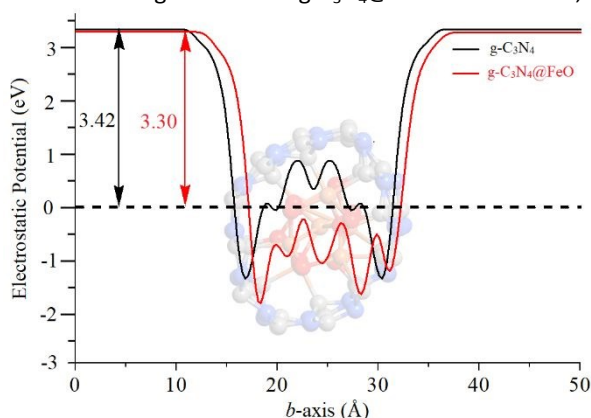


Figure 9. Averaged electrostatic potential profiles on the plane perpendicular to b-axis as a function of the b-axis of the supercell of g-C₃N₄ and g-C₃N₄@FeO, respectively. The relaxed structure of g-C₃N₄@FeO is also shown in the background.

accounts for the optimum value of ΔG_{H^*} (hydrogen adsorption) over the C in the region where FeO is sitting below and has no direct contact. Finally, this can further increase the DOS near the Fermi level and reduce the work function of the doped g-C₃N₄ (see Figure 9).

Model (II): Fe₃O₄@g-C₃N₄

As evident from our experimental results and discussion, the performance of g-C₃N₄@Fe₃O₄ system is superior to pristine g-C₃N₄; to correlate and confirm our observation, periodic DFT calculations are further carried out for Fe₃O₄, g-C₃N₄, and Fe₃O₄@g-C₃N₄ heterostructure. A lower lattice mismatch of 5.6 % is present in Fe₃O₄@g-C₃N₄ system, which also validates the co-existence between Fe₃O₄ and g-C₃N₄. The optimized structures of monolayer Fe₃O₄, g-C₃N₄, and Fe₃O₄@g-C₃N₄ are

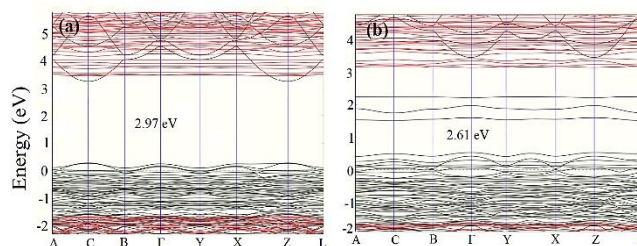


Figure 10. Simulated spin up band structures of (a) Fe₃O₄ and (b) Fe₃O₄@g-C₃N₄.

given in Figure 1c-e. It is found that g-C₃N₄ forms a non-covalent type interaction with the surface atoms of Fe₃O₄ through N-Fe with a simulated distance of ~2.2 Å; which reveals the strong electrostatic interaction in the Fe₃O₄@g-C₃N₄ system. The simulated adsorption energy of g-C₃N₄ nanosheet over Fe₃O₄ is -0.73 eV which further confirms the stability of Fe₃O₄@g-C₃N₄ heterojunction. This interface adhesion formation energy was calculated according to Equation 1.

$$\Delta E_{ad} = E_{Fe_3O_4@g-C_3N_4} - (E_{g-C_3N_4} + E_{Fe_3O_4}) \quad (1)$$

where $E_{Fe_3O_4@g-C_3N_4}$, $E_{g-C_3N_4}$, and $E_{Fe_3O_4}$ represent the total energy of the relaxed Fe₃O₄@g-C₃N₄ heterojunction, monolayer g-C₃N₄, and Fe₃O₄ slab, respectively. The interface binding energy between g-C₃N₄ monolayer and Fe₃O₄ of the heterostructure (-0.73 eV), predicts strong electrostatic interaction. Furthermore, to correlate the experimental performance of Fe₃O₄@g-C₃N₄

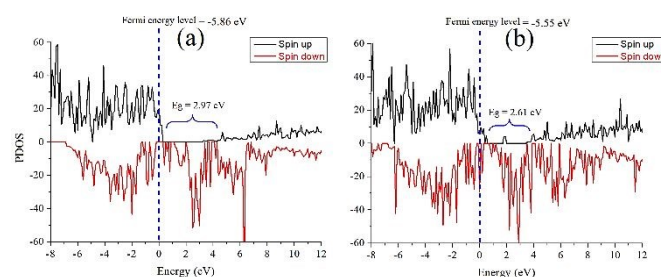


Figure 11. Partial density of state plots of (a) Fe₃O₄ and (b) Fe₃O₄@g-C₃N₄; here the bandgap of spin-up states is shown. The vertical dashed lines represent the Fermi energy level, and the energy is in eV versus vacuum.

heterostructure, the electronic properties such as band structure, DOS, and EDD of Fe₃O₄@g-C₃N₄ heterostructure are simulated. The spin-up band structures of Fe₃O₄ and Fe₃O₄@g-C₃N₄ are shown in Figure 10, where the bandgap of pristine Fe₃O₄ is 2.97 eV whilst that of Fe₃O₄@g-C₃N₄ is 2.61 eV. The combined spin and down band structures of these species are shown in Figure S6 of the Supporting Information.



The bandgaps of these species are simulated from the PDOS as well, as shown in Figure 11. Comparative analysis of the band structures of both pristine Fe_3O_4 and $\text{Fe}_3\text{O}_4@\text{g-C}_3\text{N}_4$ shows that $\text{g-C}_3\text{N}_4$ produces some extra bands in the bandgap of Fe_3O_4 . These extra bands can be called flat bands which work as charge trapping centres and consequently increase the overall catalytic performance of $\text{Fe}_3\text{O}_4@\text{g-C}_3\text{N}_4$. Interestingly, in either spin states, the Fermi energy level is diffused in the valance band (Figure 10).

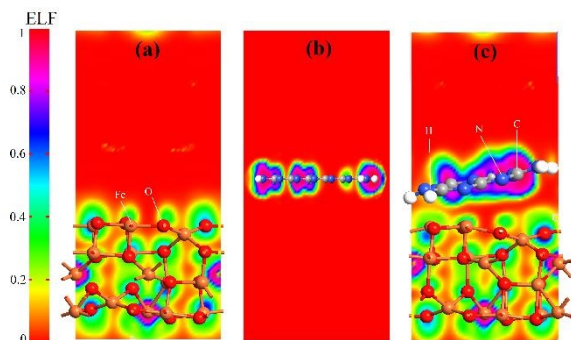


Figure 12. Electrostatic potential maps of (a) Fe_3O_4 , (b) a monolayer of $\text{g-C}_3\text{N}_4$, and (c) $\text{Fe}_3\text{O}_4@\text{g-C}_3\text{N}_4$ heterojunction.

The simulated electrostatic potential maps of Fe_3O_4 , $\text{g-C}_3\text{N}_4$, and $\text{Fe}_3\text{O}_4@\text{g-C}_3\text{N}_4$ along the Z-direction are displayed in Figure 12; where $\text{g-C}_3\text{N}_4$ monolayer has shared its electronic cloud density with a surface of Fe_3O_4 in $\text{Fe}_3\text{O}_4@\text{g-C}_3\text{N}_4$. The work functions of Fe_3O_4 , $\text{g-C}_3\text{N}_4$, and $\text{Fe}_3\text{O}_4@\text{g-C}_3\text{N}_4$ are 5.86, 4.24, and 5.55 eV, respectively. We can see that the heterojunction $\text{Fe}_3\text{O}_4@\text{g-C}_3\text{N}_4$ has optimum work; lower than that of Fe_3O_4 but higher than

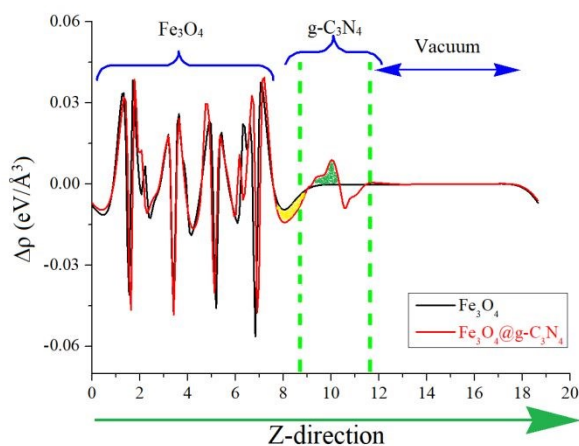


Figure 13. Average electron density difference ($\Delta\rho$) along the Z-direction for (a) Fe_3O_4 and (b) $\text{Fe}_3\text{O}_4@\text{g-C}_3\text{N}_4$. The green and yellow shaded areas indicate electron accumulation and donation, respectively.

that of $\text{g-C}_3\text{N}_4$. So, the HER performance of $\text{Fe}_3\text{O}_4@\text{g-C}_3\text{N}_4$ heterojunction can be calculated from the difference of work functions. It is also inferred that charge transferred occurred between Fe_3O_4 and $\text{g-C}_3\text{N}_4$. Finally, this type of charge transfer creates a local dipole near the interface, decreases the work function (from 5.86 to 5.55 eV) and enhances the HER activity over the surface of $\text{g-C}_3\text{N}_4@\text{FeO}$.

The charge transferring phenomena at the $\text{Fe}_3\text{O}_4@\text{g-C}_3\text{N}_4$ heterojunction is calculated from the electron difference density (EDD) of the heterostructure, and the results are shown in Figures 13 and S7. In Figure 13, the charge difference at the interface is clearly depicted where the green and yellow shaded areas represent the charge accumulation and depletion, respectively. It is found that charge distribution mainly occurs

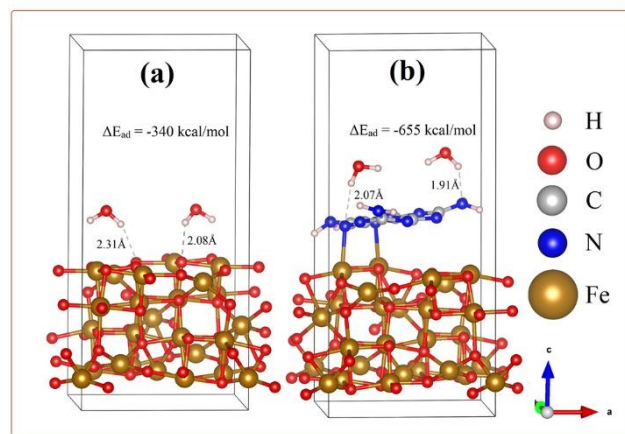


Figure 14. Relaxed geometric structures of $\text{Fe}_3\text{O}_4/\text{H}_2\text{O}$ and (b) $\text{Fe}_3\text{O}_4@\text{g-C}_3\text{N}_4/\text{H}_2\text{O}$.

at the interface region of $\text{Fe}_3\text{O}_4@\text{g-C}_3\text{N}_4$ heterostructure, whereas almost no perturbation was observed in the rest of $\text{Fe}_3\text{O}_4@\text{g-C}_3\text{N}_4$; especially those parts which are far away from the interface. We can predict that this type of charge distribution may result in a non-bonding interaction²⁷, between $\text{g-C}_3\text{N}_4$ and Fe_3O_4 (vide supra). A slice of the planar-averaged EDD along the Z-direction of Fe_3O_4 and $\text{Fe}_3\text{O}_4@\text{g-C}_3\text{N}_4$ are depicted in Figure 13 and the electron density (ED) maps are shown in Figure S7. The charge redistribution at the interface of $\text{Fe}_3\text{O}_4@\text{g-C}_3\text{N}_4$ heterostructure lead us to conclude the charge separation of electrons and holes. The amount of charge density is calculated from Bader charge analysis which is about 0.068 electrons. Furthermore, this charge accumulation and donation may result in an electric field at the interface of $\text{Fe}_3\text{O}_4@\text{g-C}_3\text{N}_4$ heterostructure which is further responsible for the separation of electrons and holes.

To determine and compare the HER performance of Fe_3O_4 and $\text{Fe}_3\text{O}_4@\text{g-C}_3\text{N}_4$, two water molecules were interacted on their surfaces, and optimized the resulted systems. The relaxed geometric structures of $\text{Fe}_3\text{O}_4/\text{H}_2\text{O}$ and $\text{Fe}_3\text{O}_4@\text{g-C}_3\text{N}_4/\text{H}_2\text{O}$ are shown in Figure 14, where H atoms of H_2O have built inter-hydrogen bonding with O of Fe_3O_4 and N of $\text{Fe}_3\text{O}_4@\text{g-C}_3\text{N}_4$, respectively.

The adsorption energy of water molecule was calculated by subtracting the energies of optimized water molecule and adsorbent bare slab (E_{surface}), from the optimized water-slab complex (surface@ H_2O), using Equation 2.

$$\Delta E_{\text{ad}} = E_{\text{surface}@H_2O} - (E_{H_2O} + E_{\text{surface}}) \quad (2)$$

The strength of hydrogen bonding in these species is calculated from inter-bonding distance and adsorption energy. As can be



ARTICLE

visualized from Figure 14, only one of the hydrogens in water interacts with the surface atoms of either Fe_3O_4 or $\text{Fe}_3\text{O}_4/\text{g-C}_3\text{N}_4/\text{H}_2\text{O}$. In case of $\text{Fe}_3\text{O}_4/\text{H}_2\text{O}$, the average hydrogen bonding distance is about 2.20 Å while the energy of this bonding is about -339.91 kcal/mol. On the other hand, the average hydrogen bonding distance in $\text{Fe}_3\text{O}_4/\text{g-C}_3\text{N}_4/\text{H}_2\text{O}$ is about 1.99 Å, which is shorter than that of the $\text{Fe}_3\text{O}_4/\text{H}_2\text{O}$ system. Moreover, the adsorption energy of water molecule in $\text{Fe}_3\text{O}_4/\text{g-C}_3\text{N}_4/\text{H}_2\text{O}$ system is about -655.15 kcal/mol which is almost doubled that of $\text{Fe}_3\text{O}_4/\text{H}_2\text{O}$. The stronger the hydrogen bonding, the higher will be the water splitting ability. The high adsorption energy of water can be correlated to experimentally lower overpotential of HER. In summary, $\text{Fe}_3\text{O}_4/\text{g-C}_3\text{N}_4$ has higher catalytic activity (in term of strong water adsorption energy) than that of pristine Fe_3O_4 . Again, these results and discussion strongly corroborate our experimental data, presented below.

Electrochemical Properties

As shown in Figure 15a, $\text{Fe}_5\text{-NC}$ exhibits a small onset potential of 73 mV and low overpotential (η_{10}) of 191 mV to achieve a current density of 1 and 10 mA cm^{-2} , respectively, which is lower than the onset potential and overpotential of both $\text{Fe}_2\text{-NC}$ and

nanocomposites of P-doped Ni@CNTs/NF , FNC-MoS_2 and $\text{Co/Co}_2\text{P@ACF/CNT HNCs}$.^{4, 28, 29} DOI: 10.1039/D1TC01022K

Corresponding Tafel plots derived from polarization curves were used to deduce the HER mechanism of the samples (Figure 15b). $\text{Fe}_5\text{-NC}$ has a small Tafel slope of 69 mV dec^{-1} , compared to $\text{Fe}_2\text{-NC}$ (77 mV dec^{-1}) and $\text{Fe}_{10}\text{-NC}$ (91 mV dec^{-1}), which indicates its faster kinetics towards HER. Based on the Tafel slope values, HER with $\text{Fe}_x\text{-NC}$ samples likely proceeded via the Volmer-Heyrovsky mechanism in which the rate limiting step is usually the electrochemical discharge step. The Tafel slope of the Volmer reaction ($\text{H}_2\text{O} + \text{e}^- \rightarrow \text{H}_{\text{ads}} + \text{OH}^-$) which represents the initial discharge step is 120 mV dec^{-1} while the electrochemical desorption, Heyrovsky reaction ($\text{H}_{\text{ads}} + \text{H}_2\text{O} + \text{e}^- \rightarrow \text{H}_2 + \text{OH}^-$) and recombination (Tafel reaction: $\text{H}_{\text{ads}} + \text{H}_{\text{ads}} \rightarrow \text{H}_2$) occurs at lower values of 40 and 30 mV dec^{-1} , respectively.³⁰ Tafel slopes of the $\text{Fe}_x\text{-NC}$ samples lie within this range, which suggests that Volmer-Heyrovsky mechanism must have occurred during hydrogen evolution.

Cyclic voltammetry at different scan rates (5 - 50 mV s^{-1}) was applied to study the electrochemical properties of $\text{Fe}_x\text{-NC}$ samples and the results are presented in Figure 15c. Reaction profile was capacitive rather than Faradaic during volumetric scan within the range of -0.1 - 0 V (vs RHE). The electrochemical active surface areas (ESCA) of the three samples were evaluated by measuring the double layer capacitance (C_{dl}) obtained from a fitting of the difference in current densities versus the scan rates. From Figure 15d, the C_{dl} of $\text{Fe}_2\text{-NC}$, $\text{Fe}_5\text{-NC}$ and $\text{Fe}_{10}\text{-NC}$ were determined to be 11.12, 23, and 15 mF cm^{-2} , respectively. The improved C_{dl} value for $\text{Fe}_5\text{-NC}$ is linked to its improved electrocatalytic performance due to the presence of intrinsically more catalytically active sites. Reaction kinetics of $\text{Fe}_x\text{-NC}$ samples at the electrode/electrolyte interface was evaluated by EIS. The Nyquist plots in Figure 15e reveal that the charge transfer resistance (R_{ct}) of $\text{Fe}_5\text{-NC}$ (8 Ω) is much lower than that of the other samples ($\text{Fe}_2\text{-NC}$, 14 Ω and $\text{Fe}_{10}\text{-NC}$, 44 Ω) which indicates a faster kinetics and reaction process, due to easier charge transfer at the electrode/electrolyte interface. Stability of $\text{Fe}_5\text{-NC}$ was measured by chronoamperometric curves and taking continuous linear potential sweeps on the electrode at a scan rate of 50 mV s^{-1} for 5000 cycles. As shown in Figure 15f, the current density of $\text{Fe}_5\text{-NC}$ exhibits negligible changes after 5000 cycles compared with the initial curve, with only minimal loss of activity at a current density of 10 mA cm^{-2} . The chronoamperometric curve recorded at -0.3 V in Figure S9 also indicates that $\text{Fe}_5\text{-NC}$ retains 94% of its relative current density after 5 hours of testing. This result demonstrates the improved stability of $\text{Fe}_5\text{-NC}$ as HER electrocatalyst. Although $\text{Fe}_5\text{-NC}$ shows good stability, the dissolution of Fe ions concentration in electrolyte cannot be ruled out and will be investigated via inductively coupled plasma mass spectrometry in the future to further validate its long-term stability. The morphology and crystal structure of $\text{Fe}_5\text{-NC}$ exhibit negligible changes after 5000 cycles (Figure S8), which is indicative of its good stability. These results confirm that the present carbon nitride shell indeed can protect the oxides from acidic bubble corrosions during the cycling test, which highlights its application potentials.

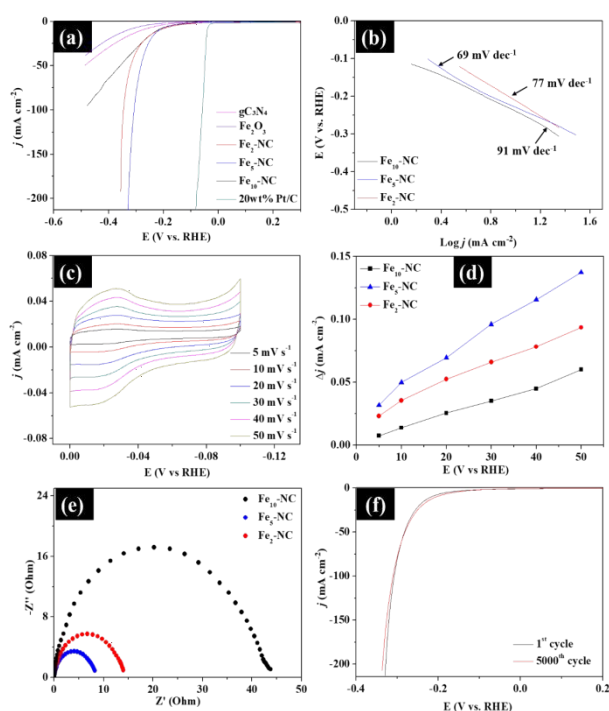


Figure 15. Electrochemical properties of $\text{Fe}_x\text{-NC}$ samples for HER. (a) Polarization curves. (b) Tafel plots. (c) Cyclic voltammograms curves at different scan rates. (d) Charging current density differences Δj plotted against scan rates, (e) Nyquist plots, and (f) Polarization curves of $\text{Fe}_5\text{-NC}$ before and after 5000 cycles.

$\text{Fe}_{10}\text{-NC}$ samples. $\text{Fe}_2\text{-NC}$ and $\text{Fe}_{10}\text{-NC}$ require overpotential of 215 mV and 233 mV to reach 10 mA cm^{-2} . The LSV curves also indicate that $\text{Fe}_5\text{-NC}$ exhibits better activity with higher catalytic currents compared with the other samples. These results are comparable to recently reported metal encapsulated



To sum up, the enhanced catalytic activity of Fe₅-NC can be attributed to the following reasons: (1) synergy between iron oxide nanoparticles and the graphitic carbon nitride shell which promotes HER activity by facilitating faster charge transfer and weakening strong hydrogen adsorption to obtain improved hydrogen desorption; (2) uniform distribution of all elements and creation of abundant defect sites from the N-doping into carbon frameworks which would improve interfacial adsorption and electronic interaction while creating catalytically active sites for the HER activity; (3) the introduction of high ESCA which allows for enhanced accessibility of exposed active sites for HER; and (4) the smaller charge transfer resistance linked to the faster kinetics and higher current density.

Conclusions

Fe_x-NC nanocomposites were successfully prepared via a simple method using melamine as the simultaneous nitrogen and carbon source. The resulting Fe_x-NC consists of iron oxide nanoparticles sheathed by graphitic carbon nitride shells of 8.1 - 30 nm thick. The observed data of g-C₃N₄ encapsulated iron oxide nanoparticles were successfully reproduced with the help of periodic density functional theory (DFT) simulations. Both theory and experiment strongly correlate to each other, where the g-C₃N₄@FeO has superior performance compared to pristine g-C₃N₄ and Fe₃O₄. It is found that the catalytic activity of g-C₃N₄@FeO arise from the electron transfer from FeO particles to the g-C₃N₄ which forms an electrostatic interaction, leading to a decreased local work function on the surface of g-C₃N₄ which consequently enhanced the HER activity.

Conflicts of interest

The authors have no competing interest to declare.

Acknowledgements

O. Ola is grateful for the support from the Leverhulme Trust Early Career Fellowship, ECF-2018-376.

References

1. F. Safizadeh, E. Ghali and G. Houlachi, *Int. J. Hydrogen Energy*, 2015, **40**, 256-274.
2. J. Lu, S. Yin and P. K. Shen, *Electrochem Energy Rev*, 2019, **2**, 105-127.
3. G. Hu, J. Li, P. Liu, X. Zhu, X. Li, R. N. Ali and B. Xiang, *Appl. Surf. Sci.*, 2019, **463**, 275-282.
4. S. Jing, D. Wang, S. Yin, J. Lu, P. K. Shen and P. Tsiakaras, *Electrochim. Acta*, 2019, **298**, 142-149.
5. Y. Yao, H. Chen, J. Qin, G. Wu, C. Lian, J. Zhang and S. Wang, *Water Res.*, 2016, **101**, 281-291.
6. Y. G. Zhu, J. Xie, G. S. Cao, T. J. Zhu and X. B. Zhao, *RSC Advances*, 2013, **3**, 6787-6793.
7. M. Huck, L. Ring, K. Küpper, J. Klare, D. Daum and H. Schäfer, *Journal of Materials Chemistry A*, 2020, **8**, 9896-9910.
8. B. H. Suryanto, Y. Wang, R. K. Hocking, W. Adamson and C. Zhao, *Nature communications*, 2019, **10**, 1-10.
9. M. Wang, C. Zhang, T. Meng, Z. Pu, H. Jin, D. He, J. Zhang and S. Mu, *J. Power Sources*, 2019, **413**, 367-375.
10. AtomistixToolKit, (www.quantumwise.com).
11. VirtualNanoLab, (www.quantumwise.com).
12. M. Iizumi, T. Koetzle, G. Shirane, S. Chikazumi, M. Matsui and S. Todo, *Acta Crystallographica Section B: Structural Crystallography and Crystal Chemistry*, 1982, **38**, 2121-2133.
13. A. H. Larsen, M. Vanin, J. J. Mortensen, K. S. Thygesen and K. W. Jacobsen, *Phys. Rev. B*, 2009, **80**, 195112.
14. G. Kresse and D. Joubert, *Phys. Rev. B*, 1999, **59**, 1758.
15. X. Guo, G. Yue, J. Huang, C. Liu, Q. Zeng and L. Wang, *ACS Appl Mater Interfaces*, 2018, **10**, 26118-26127.
16. G. Raj, A. Bhagi and V. Jain, *Group theory and Symmetry in Chemistry*, Krishna Prakashan Media, 2010.
17. A. Ferrari, S. Rodil and J. Robertson, *Physical Review B*, 2003, **67**, 155306.
18. A. Stolz, S. Le Floch, L. Reinert, S. M. Ramos, J. Tuillon-Combes, Y. Soneda, P. Chaudet, D. Baillis, N. Blanchard and L. Duclaux, *Carbon*, 2016, **107**, 198-208.
19. A. Rufus, N. Sreeju and D. Philip, *RSC advances*, 2016, **6**, 94206-94217.
20. L. Nalbandian, E. Patrikiadou, V. Zaspalis, A. Patrikidou, E. Hatzidaki and C. N. Papandreou, *Current Nanoscience*, 2016, **12**, 455-468.
21. Y. He, L. Huang, J.-S. Cai, X.-M. Zheng and S.-G. Sun, *Electrochim. Acta*, 2010, **55**, 1140-1144.
22. E. Liu, H. Yuan, Z. Kou, X. Wu, Q. Xu, Y. Zhai, Y. Sui, B. You, J. Du and H. Zhai, *Scientific reports*, 2015, **5**, 11164.
23. Y. Hou, B. Zhang, Z. Wen, S. Cui, X. Guo, Z. He and J. Chen, *Journal of Materials Chemistry A*, 2014, **2**, 13795-13800.
24. Z.-Y. Wu, X.-X. Xu, B.-C. Hu, H.-W. Liang, Y. Lin, L.-F. Chen and S.-H. Yu, *Angew. Chem. Int. Ed.*, 2015, **54**, 8179-8183.
25. H.-F. Li, F. Wu, C. Wang, P.-X. Zhang, H.-Y. Hu, N. Xie, M. Pan, Z. Zeng, S. Deng, M. H. Wu, K. Vinodgopal and G.-P. Dai, *Nanomaterials (Basel, Switzerland)*, 2018, **8**, 700.
26. J. Nørskov and T. Bligaard, *J. Electrochem. Soc.*, 2005, **152**, J23.
27. J. Liu, *J. Phys. Chem. C*, 2015, **119**, 28417-28423.
28. F. Wang, L. Hu, R. Liu, H. Yang, T. Xiong, Y. Mao, M. S. Balogun, G. Ouyang and Y. Tong, *Journal of Materials Chemistry A*, 2019, **7**, 11150-11159.
29. X. Wang, S. Fei, S. Huang, C. Wu, J. Zhao, Z. Chen, K. Uvdal and Z. Hu, *Carbon*, 2019, **150**, 363-370.
30. Y. Wang, Y. Zhu, S. Afshar, M. W. Woo, J. Tang, T. Williams, B. Kong, D. Zhao, H. Wang and C. Selomulya, *Nanoscale*, 2019, **11**, 3500-3505.
31. J. Endres, D. A. Egger, M. Kulbak, R. A. Kerner, L. Zhao, S. H. Silver, G. Hodes, B. P. Rand, D. Cahen and L. Kronik, *J. Phys. Chem. Lett.*, 2016, **7**, 2722-2729.
32. M. W. Chase, *J. Phys. Chem. Ref. Data*, 1996, **25**, 1069-1111.

